Preliminary design of control rods in the single-fluid double-zone thorium molten salt reactor (SD-TMSR)

O. Ashraf [a,b,*], Andrei Rykhlevskii [c], G.V. Tikhomirov [a], Kathryn D. Huff [c]

[a] *Dept. of Theoretical and Experimental Physics of Nuclear Reactors, Institute of Nuclear Physics and Engineering, National Research Nuclear University MEPhI, 31, Kashirskoe Shosse, Moscow 115409, Russian Federation*
[b] *Physics Department, Faculty of Education, Ain Shams University, Cairo 11341, Egypt*
[c] *Dept. of Nuclear, Plasma, and Radiological Engineering, University of Illinois at Urbana-Champaign, Urbana, IL 61801, United States*

ARTICLE INFO

ABSTRACT

Recent studies on Molten Salt Reactors (MSRs) showed that the excess reactivity at the beginning of the operation is large for many fueling strategies and must be compensated by a reactivity control system. The current work introduces a reliable safety system based on control rods in addition to the online feed system reactivity control in the Single-fluid Double-zone Thorium-based Molten Salt Reactor (SD-TMSR). Three different initial fissile loadings are considered: ^{233}U, reactor-grade Pu, and transuranic (TRU) elements as a startup fuel. We applied six different absorbing materials to investigate the main operational and safety parameters in the SD-TMSR: natural B_4C, enriched B_4C with 90% ^{10}B, HfB_2, $HfH_{1.62}$, Eu_2O_3, and Gd_2O_3. The present work focuses on control rod design, integral and differential control rod worth, shutdown margin, and shadowing effects at steady-state. We employed the SERPENT-2 Monte-Carlo code to calculate the reactivity worth and analyze the performance of the reactivity control system. We showed that ^{233}U and reactor-grade Pu startup cores maintain adequate shutdown margin with all considered absorbers. Finally, this paper proposes a design of control rod clusters that compensate the excess reactivity of the SD-TMSR loaded with different initial fissile material.

© 2020 Elsevier Ltd. All rights reserved.

1. Introduction

The Generation IV International Forum (GIF) (DOE, 2002) determined six innovative reactor systems for further research and commercialization: the Very High-Temperature Reactor (VHTR), the Molten Salt Reactor (MSR), the Supercritical Water-Cooled Reactor (SWCR), the Gas-cooled Fast Reactor (GFR), the Sodium-cooled Fast Reactor (SFR), and the Lead-cooled Fast Reactor (LFR). The MSR is the only liquid-fueled reactor among these reactors. Major nuclear centers are pursuing MSRs with renewed interest (Betzler et al., 2019; Ashraf et al., 2020) due to its potential advantages, for example, thorium fuel utilization, small waste production, and ability to use spent fuel. However, this technology has difficulties including safety, online reprocessing, and fuel handling. The unique characteristics of the MSR (liquid fuel, flux level, neutron economy, etc.) strongly affect its control system design. Doppler effect and

thermal expansion of the fuel reduce core reactivity when the core heats up, thus MSRs have negative total temperature coefficient of reactivity (Nuttin et al., 2005). MSR designs have drain tanks to hold and cool down the liquid fuel in an emergency. In some MSR design concepts, a freeze plug, which is located under the core, passively melts when the fuel temperature reaches a critical point, and drains the fuel salt from the reactor vessel to the drain tanks. The drain tanks have a subcritical configuration with a large free surface area to readily dissipate heat by passive cooling (Elsheikh, 2013).

At the Beginning of Life (BOL), MSRs are commonly loaded with more fuel than that required to achieve criticality (necessary for long-term core operation); this leads to excess reactivity at the BOL. Robertson et al. analyzed the Molten Salt Breeder Reactor (MSBR) loaded by ^{233}U/^{232}Th fuel and concluded that two graphite rods are sufficient for adjusting reactivity during operation due to a small reactivity swing. Robertson et al. also reported that two safety rods made of boron carbide (B_4C) are enough to safely shut the MSBR down from any state (Robertson, 1971). However, the ^{233}U supply for commercial power plants is not readily available. Our recently published paper (Ashraf et al., 2020) concluded that for realistic fueling scenarios (e.g., enriched U/^{232}Th, TRU/^{232}Th,

* Corresponding author at: Dept. of Theoretical and Experimental Physics of Nuclear Reactors, Institute of Nuclear Physics and Engineering, National Research Nuclear University MEPhI, 31, Kashirskoe Shosse, Moscow 115409, Russian Federation.
E-mail addresses: osama.ashraf@edu.asu.edu.eg, oabdelaziz@mephi.ru (O. Ashraf).

and Pu/^{232}Th), large excess reactivity is required. Betzler et al. also reported large excess reactivity in Transatomic Power Molten Salt Reactor (TAP MSR) to ensure a 30-year operation cycle (Betzler et al., 2017). Additionally, Rykhlevskii et al. studied the fuel cycle performance for various Fast-Spectrum MSR designs. For a fast MSRs, a considerable excess reactivity is also required for long-term core operation (Rykhlevskii et al., 2019). Recent studies on MSRs showed that the excess reactivity at the BOL may vary from 1.2% for ^{233}U-loaded core (Rykhlevskii et al., 2019; Betzler et al., 2016) to 8.1% for Pu/TRU-loaded core (Ashraf et al., 2020).

The online reprocessing and refueling system is designed to operate as a long-term reactivity control in the MSRs (Ashraf et al., 2019; Ashraf and Tikhomirov, 2020). However, we cannot rely on online reprocessing to adjust reactivity quickly, because loop time (time needed for one particle to make one full circulation through the primary loop) is approximately 20 s for MSBR and its analogs. Consequently, we need a prompt reactivity control system for emergencies. The most common and reliable way to control the reactivity is to insert or withdraw control rods made of a material with a large neutron absorption cross section (e.g., boron). Insertion of control rods introduces negative reactivity into the core which helps to compensate the excess reactivity and adjust the power level of the core or shut down the reactor in case of emergency. Therefore, we should estimate the reactivity worth of the control rods. The reactivity worth of control rods correlates with the interference (shadowing effects) between control rod clusters (Čerba et al., 2017). The control rod worth and its efficiency in compensating excess reactivity is a subject of significant interest since it directly affects the reactor safety (Atkinson et al., 2019). Additionally, the Nuclear Regulatory Commission (NRC) prescribes that one of two independent reactivity control systems should use control rods (Criterion 26) (Commission et al., 1987). According to the demands of nuclear safety regulations, two independent shutdown systems must ensure the reactor safe operation, adjust power, and ensure the shutdown of the reactor anytime independently. All the shutdown systems must be sufficient to shut down the reactor at any time during operation.

Boron carbide (B_4C) is a commonly used material for the control rods; however, we may need to enrich the boron isotope (^{10}B) to reach the necessary absorption cross section. Additionally, issues related to helium gas release through (n,α) reactions of ^{10}B, high loss of the absorption ability under irradiation, and swelling limit the B_4C lifespan (Guo et al., 2019). Guo (2019), Gosset (2017), and Rudy (2011) summarized the properties of the potential alternative absorbers for Generation-IV reactors such as hafnium-based materials and rare earth oxides. These absorbers have high thermal conductivity, good resistance to neutron irradiation, and absorb neutrons mainly through (n,γ) reactions (Guo et al., 2019).

The SD-TMSR with a thermal power of 2,250 MW$_{th}$ (Li et al., 2018) is a graphite-moderated molten salt reactor. Adjusting fertile and fissile feed rates helps to control the reactivity of the SD-TMSR (Ashraf et al., 2020; Li et al., 2018). However, a reactivity control system for maneuvering and emergency shutdown in the SD-TMSR has not been introduced in the literature (Li et al., 2018; Zou et al., 2018; Zhang et al., 2020). Therefore, the main objective of our study is to introduce a new, rapid reactivity control system based on control rods in the SD-TMSR to control the reactivity during normal operation and shut down the reactor in case of emergency. Six absorbing material options are considered in the context of the neutronics and safety parameters in the SD-TMSR. We focus on control rod design, absorption ability, integral and differential control rod worths, shutdown margin, and shadowing effects at steady-state calculation.

Xuemei and Guimin (2013) calculated the control worth in the thorium molten salt reactor by using MCNP (Briesmeister et al., 2000). We adopted the SD-TMSR core geometry optimized by Li et al. (2018) which is different from the Molten Salt Breeder Reactor-like geometry by Mathieu et al. (2006) adopted by Xuemei and Guimin (2013). Additionally, Xuemei et al. studied the natural B_4C as absorbing material while we considered six different absorbing materials.

Čerba et al. (2017) designed a reactivity control system for the GFR. They utilized the MCNP (Briesmeister et al., 2000) and KENO6 codes (Petrie and Landers, 1984) to calculate the reactivity worth and analyze the performance of this control system (Čerba et al., 2017). Since no geometry design of the control rods system is available for the SD-TMSR, Čerba's methodology (Čerba et al., 2017) helped us as a starting point of this analysis.

The online reprocessing and refueling is a distinguishing feature for MSRs comparing with traditional solid fuel reactors. Its neutron characters including effective multiplication factor (k_{eff}), excess reactivity, Breeding Ratio (BR), and ^{233}U production are totally different when operating from those at startup. The k_{eff}, excess reactivity, and neutron flux are all related to the scheme of reprocessing. Therefore, the worth of the control rods should be corresponding to the reprocessing scheme; that is, the rate of extraction and addition of elements. However, the present work focuses on the steady-state calculations without taking into account fuel salt depletion.

All calculations presented in this work are performed using Monte-Carlo code SERPENT-2 version 2.1.31 (Leppänen et al., 2013). Delayed neutron precursor drift was neglected in this study.

This paper is organized as follows: Section 2 discusses the reactor and control rod design, Section 3 describes methodology and tools adopted to evaluate the control rod design, Section 4 focuses on calculated control rod parameters such as integral and differential worth, shutdown margin (SDM), and amplification factors, and Section 5 highlights the conclusions.

2. Model description

2.1. Reactor design

The Chinese Academy of Sciences started the program of Thorium Molten Salt Reactor (TMSR) in 2011 (Jiang et al., 2012), and many works have been done on the design of MSR and the use of Thorium with the Th-U fuel cycle (Li et al., 2015). Among them, the SD-TMSR is proposed in 2018 (Li et al., 2018), which is a graphite-moderated molten salt reactor with thermal power of 2,250 MW$_{th}$. The design of the SD-TMSR is inspired by the MSBR (Robertson, 1971) and the Thorium-based Molten Salt Reactor (TMSR) (Nuttin et al., 2005), which combines the advantages of high breeding ratio (BR) in fast spectrum and low fissile inventory of ^{233}U in thermal spectrum. The SD-TMSR also offers a negative and strong temperature coefficient of reactivity (Li et al., 2018). Fig. 1 illustrates the quarter-core view of the SD-TMSR. The core of the SD-TMSR is a right cylinder divided into an inner zone (486 fuel tubes) and an outer zone (522 fuel tubes) to enhance breeding performance. In this study, the fuel salt composition is LiF–BeF$_2$–(HM)F$_N$ (70–17.5–12.5 mol%), where HM is the heavy metal (i.e., ^{232}Th and fissile materials), and N depends on the chosen fissile material and the thermochemical state of the liquid fuel salt. Three different types of initial fissile materials are considered: (1) ^{233}U (Ashraf et al., 2020), (2) reactor-grade Pu (Marka, 1993), and (3) transuranic (TRU) elements from Light Water Reactor (LWR) spent nuclear fuel (SNF) (de Saint Jean et al., 2000). The reactor-grade Pu and TRU isotopic vectors are summarized in Tables 1 and 2, respectively.

The density and volume of the fuel salt are 3.3 g/cm^3 and 52.9 m^3, respectively. The liquid fuel salt circulates continuously through the channels that pierce the graphite hexagonal prisms.
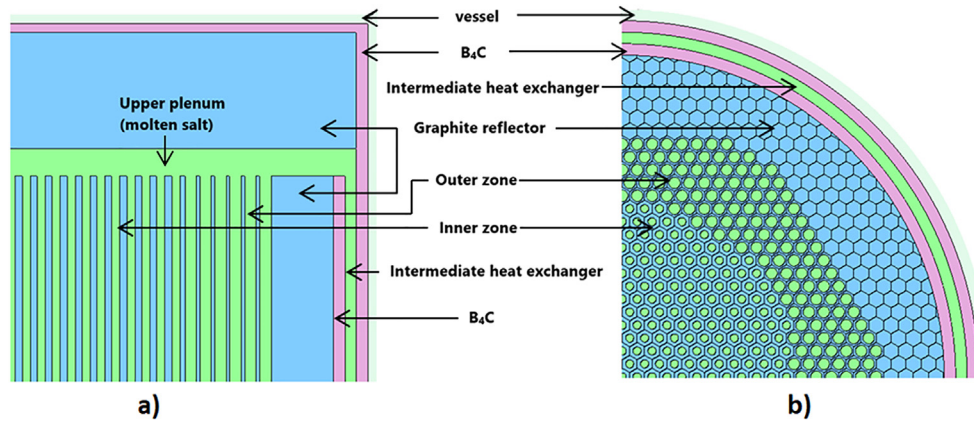
Fig. 1. *XZ* (a) and *XY* (b) section of the quarter-core model of the SD-TMSR (Ashraf and Tikhomirov, 2020).

Table 1
Reactor-grade Pu vector (wt.%) (Marka, 1993).

^{238}Pu	^{239}Pu	^{240}Pu	^{241}Pu	^{242}Pu
1.3	60.3	24.3	9.1	5

The core is surrounded by axial and radial graphite reflectors to minimize the neutron leakage. We adopted the same graphite density reported in the original SD-TMSR paper (2.3 g/cm^3) (Li et al., 2018) to be consistent with results in the literature. A 10-cm-thick B$_4$C cylinder surrounds the core to shield against neutrons and heat. Finally, the SD-TMSR pressure vessel holds all reactor components and is made of a Hastelloy N alloy. The main characteristics of the SD-TMSR are summarized in Table 3.

2.2. Control rod design

The present paper proposes two sets of rods to control the reactivity of the SD-TMSR core:

1. Control Safety Devices (CSD);
2. Shutdown Safety Devices (SSD).

The CSD system is designed for reactivity control during normal operation and the SSD system is designed for an emergency reactor shutdown. In the present work, six different absorbing materials are considered based on their neutronics and safety performance:

1. natural B$_4$C (19.9% ^{10}B);
2. B$_4$C (enriched to 90% ^{10}B);
3. hafnium diboride (HfB$_2$);
4. hafnium hydride (HfH$_{1.62}$);
5. gadolinium oxide (Gd$_2$O$_3$);
6. europium oxide (Eu$_2$O$_3$).

The assessment of the optimal absorber radius should be an essential consideration. If the CR radius is too large, the absorber material is not effectively utilized due to self-shielding. We changed the radius of the CR and calculated the corresponding k_{eff} when all CRs were fully inserted. Fig. 2 illustrates the change of the k_{eff}

Table 3
The main characteristics of the SD-TMSR (Li et al., 2018; Ashraf et al., 2020).

Thermal power, MW$_{th}$	2,250
Fuel salt components	LiF–BeF$_2$–(HM)F$_N$
Fuel composition, mole%	70–17.5–12.5
^{7}Li enrichment, %	99.995
Fuel temperature, K	900
Dilatation coefficient, g/(cm^3·K)	-6.7×10^{-4}
Fuel volume, m^3	52.9
Fuel density at 900 K, g/cm^3	3.3
Graphite density, g/cm^3	2.3
Core diameter, cm	460
Core height, cm	460
Upper plenum, cm	30
Lower plenum, cm	30
Side length of the graphite hexagonal prism, cm	7.5
Radius (inner fuel channel), cm	3.5
Radius (outer fuel channel), cm	5
Volume ratio of molten salt to graphite in the inner zone	0.357
Volume ratio of molten salt to graphite in the outer zone	1.162

with the radius of the control rod for all different materials. As shown in Fig. 2, in the region between 0.0 and 0.75 cm, the k_{eff} decreases sharply with increasing absorber radius for all absorbers. However, for the B$_4$C control rod, in the region between 0.75 and 1.0 cm, there is almost no change in the k_{eff}. This is because of the geometry self-shielding of the neutron flux; beyond r = 0.75 cm, the ^{10}B atoms in the central zone of the CR have a relatively low chance for neutron capture. In contrast, other absorbers are not affected by the self-shielding phenomenon in the considered region (0.0<r<1.0 cm). From the obtained results, we proposed the control rod as a cylinder with a radius of 0.75 cm and a height of 520 cm (core height in addition to upper and lower plenums). The absorbing material is surrounded by a 0.25-cm-thick cladding made of AIM1 (15Cr-15Ni) steel alloy (Séran and Flem, 2017) and the guide tube is made of SiC structural material (see Fig. 3). Robertson et al. suggested the thickness of the gap between the CR and graphite in MSBR of about 7% of the CR diameter (Robertson, 1971). We adopted this design solution and assumed a 0.1-cm-thick gap (~7% of the CR diameter) between the cladding and guide tube to facilitate the control rod movement. However,
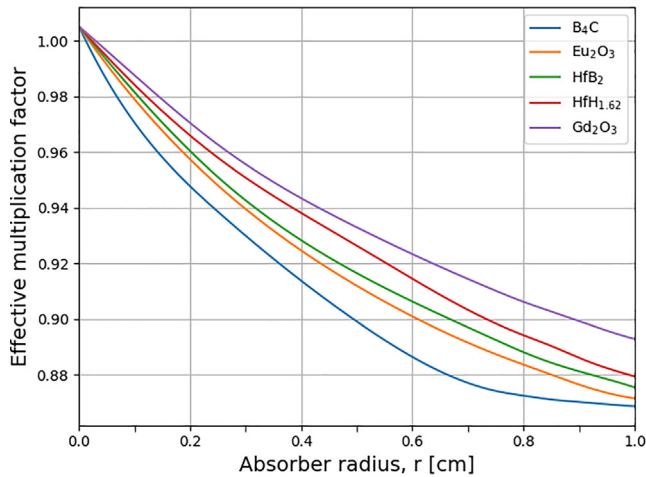
Table 2
TRU vector (wt.%) (de Saint Jean et al., 2000).

^{237}Np	^{238}Pu	^{239}Pu	^{240}Pu	^{241}Pu	^{242}Pu	^{241}Am	^{243}Am	^{244}Cm	^{245}Cm
6.3	2.7	45.9	21.5	10.7	6.7	3.4	1.9	0.8	0.1

Fig. 2. The change of the effective multiplication factor with the radius of the control rod for all different absorbers.

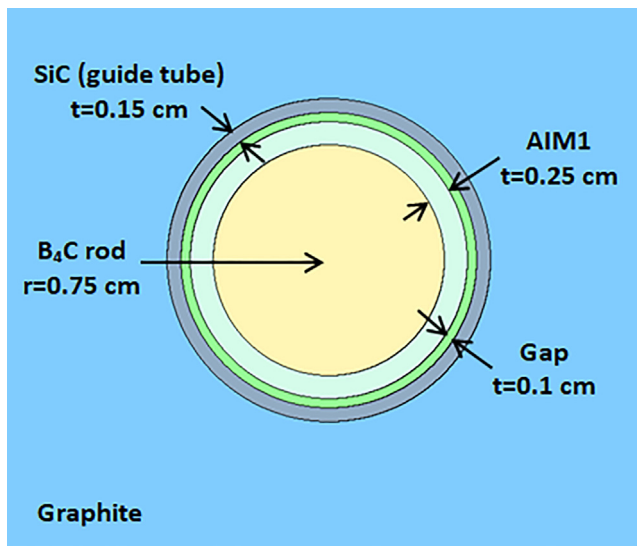**Fig. 3.** Cross section of the B_4C control rod.

Fig. 4. XY section of graphite element with the four control rods (cluster) located at the same distance from the fuel channel.

the absorber-cladding gap was neglected for simplicity. Thermal emission and corresponding thermal–hydraulics simulations to predict the temperature of the salt around CRs are out of the scope of this study and will be covered in future work. All densities of rod materials are listed in Table 4.

Since the total number and distribution of the control assemblies in the SD-TMSR have not been determined, we propose an original distribution as a starting point of this analysis. We added clusters consisting of four control rods to specific graphite hexagonal prisms (elements) in the SD-TMSR core. Every four control rods can move together as one group (cluster). Fig. 4 demonstrates the
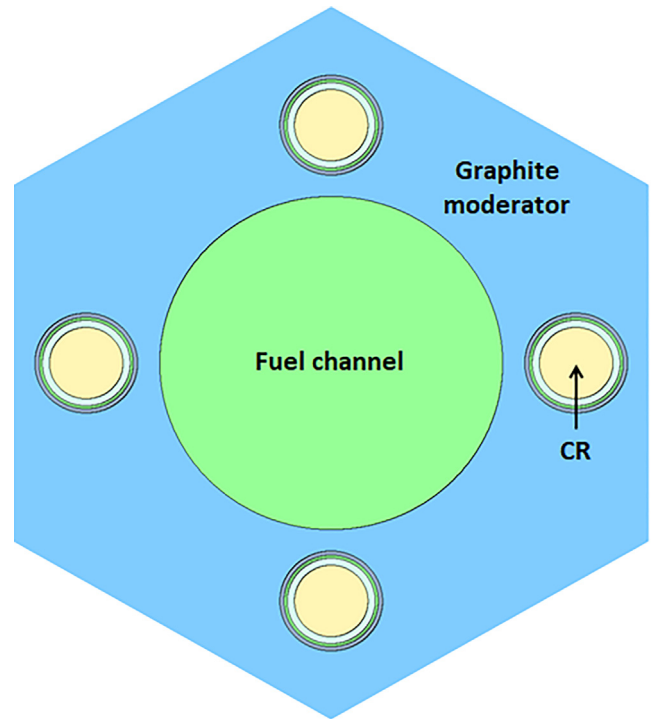
Table 4
The densities of the absorbing materials.

Absorbers	Density [g/cm^3]
B_4C	2.54
HfB_2	10.5
$HfH_{1.62}$	11.4
Gd_2O_3	7.04
Eu_2O_3	7.38
SiC	3.21
AIM1 cladding	7.987

plan view of the graphite element with the control rods. We propose 25 graphite elements with control rods: 16 Control Safety Devices (CSD) and 9 Shutdown Safety Devices (SSD). We distributed the 25 graphite elements with control rod clusters uniformly in the inner core of the SD-TMSR, in which the moderator-to-fuel ratio is high.

Fig. 5 illustrates the numbering scheme of control rod clusters in the SD-TMSR core. The CSD1-16 clusters are represented as yellow and distributed as two rings: inner and outer (peripheral) ring. The inner ring includes CSD from 1 to 6, while the outer ring includes CSD from 7 to 16. Red stands for SSD1-9 clusters. The selected core segment at the upper left corner of Fig. 5 shows that both CSD and SSD clusters consist of four control rods located at the same distance from the fuel channel center.

3. Methodology and tools

3.1. Control rod design evaluation

In this work, SERPENT-2 (Leppänen et al., 2013) is used to perform steady-state calculations for a full 3D model of the SD-TMSR with the suggested control rod design. We adopted the ENDF/B-VII.0 (Chadwick et al., 2006) cross section library for all calculations in the present work. The results demonstrated in this study were obtained after full-core calculations simulating 25×10^6 active neutron histories per cycle. Simulations consisted in 500 active cycles of 5×10^4 neutrons subdivided in 8 parallel tasks. Each simulation skipped 50 inactive cycles before beginning active tallies to allow for the convergence of the fission source distribution. Convergence has been checked through the fission source entropy. The statistical error in k_{eff} was $\leqslant 25$ pcm.

The initial calculation state of the SD-TMSR is identified by normal operation conditions (see Table 3) and fully withdrawn control rod clusters. In this case, the control rods are located above the
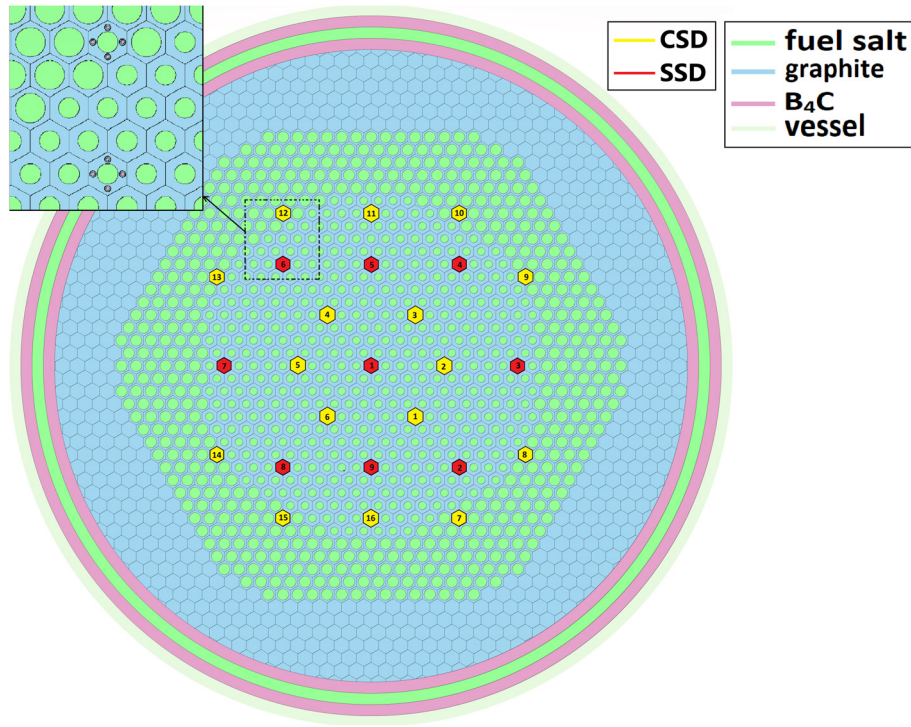
Fig. 5. Distribution of the graphite elements with CRs in the SD-TMSR core.

upper plenum as shown in Fig. 6. To validate the proposed control rods system we adopted the same operation conditions (as in the initial calculation state) and changed the position of the control rod clusters along the Z direction. The main calculated parameters including reactivity, control rod worth, and interference effects (shadowing effects) are described below.

3.1.1. Reactivity calculation

The excess reactivity ρ_e is the reactivity of the core when all control rods are withdrawn. ρ_e is calculated by SERPENT-2 based on Eq. 1, where k_{eff} is the effective multiplication factor of the core:

$$\rho_e = \frac{k_{eff} - 1}{k_{eff}}. \tag{1}$$

3.1.2. The control rod worth (CRW)

The control rod worth (CRW) is the amount of negative reactivity associated with the control rod insertion. The CRW is calculated by SERPENT-2 based on Eq. 2, where $\Delta\rho_{CRi}$ is the worth of the ith control rod (CR), ρ_e is the initial excess reactivity, and ρ_{CRi} is the excess reactivity after insertion of the ith CR (Čerba et al., 2017):

$$\Delta\rho_{CRi} = \rho_e - \rho_{CRi}. \tag{2}$$

3.1.3. Shutdown margin (SDM)

The shutdown margin (SDM) is the amount of reactivity by which a full reactor core is subcritical from a given state. The Shutdown Safety Devices (SSD) clusters are designed mainly for an emergency shutdown, thus it should provide the reactor core with sufficient negative reactivity. The SDM is expressed in terms of reactivity and calculated by Eq. 3, where $\Delta\rho_{SSD}$ is the total worth of the Shutdown Safety Devices (SSD) and ρ_e is the core excess reactivity:
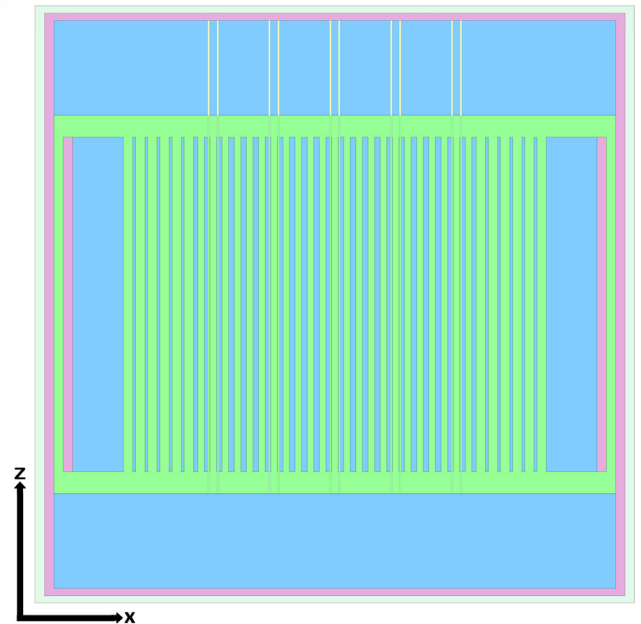
$$SDM = \Delta\rho_{SSD} - \rho_e. \tag{3}$$

Fig. 6. XZ view at the midplane of the full-core model of the SD-TMSR, 10 CRs are fully withdrawn.

3.1.4. Interference effects (shadowing effects)

Interference between control rods (CRs) or shadowing effects occur when one (or more) control rod impacts the reactivity worth of another control rod in the surroundings. The insertion of a CR depresses the neutron flux in its vicinity and makes the curvature of the neutron flux greater. The gradient of the neutron flux will contrarily increase at a radial distance. The CRs, distributed in the core, will distort the neutron flux around each other and will impact the reactivity worth. The term "shadowing effect" has been

used to describe this phenomenon (Oka et al., 2014). The shadowing effect appears when the combined rod worth is less than the sum of the individual worths. Meanwhile, anti-shadowing is observed when the combined rod worth is greater than the sum of the individual worths. The core height-to-diameter ratio (H/D), CR locations, and the three-dimensional configuration of the CRs affect the degree of the interference between CRs (Oka et al., 2014).

The amplification factor of the ith CR (A_{CRi}) helps to evaluate the shadowing effects between CR clusters. The A_{CRi} is calculated by Eq. 4 (Čerba et al., 2017), where $\Delta\rho_{CR(1,2,...N)}$ is the total worth of all CRs (from 1 to N), $\Delta\rho_{CR(1,2,...N-i)}$ is the total worth of all CRs except the ith rod, and $\Delta\rho_{CRi}$ is the worth of the ith rod:

$$A_{CRi} = \frac{\Delta\rho_{CR(1,2,...N)} - \Delta\rho_{CR(1,2,...N-i)}}{\Delta\rho_{CRi}}. \tag{4}$$

If A_{CRi} is <1, the CRW is reduced due to shadowing effects, but if A_{CRi} is >1, the CRW is amplified and anti-shadowing effects occur (Girardin et al., 2007). A_{CRi} = 1 means no shadowing effects occur.

3.1.5. Integral and differential control rod worth

The integral CRW is the total reactivity change due to the full insertion or withdrawal of the CR. However, the *differential CRW* is the reactivity inserted per unit of withdrawal [pcm/cm]. To calculate those parameters, we varied the position of CR clusters from fully withdrawn to fully inserted. Eq. 5 is used to calculate the integral CRW [pcm], where k_{j-1} and k_j are the effective multiplication factors before and after CR insertion to the jth step, respectively, and N is the number of steps:

$$\Delta\rho_j = \sum_{j=1}^{N} \frac{k_j - k_{j-1}}{k_j k_{j-1}}. \tag{5}$$

Eq. 6 is used to calculate the theoretical differential CRW, where ΔZ is the length of rod inserted:

$$\frac{\partial\rho_j}{\partial Z} = \frac{1}{\Delta Z}\frac{k_j - k_{j-1}}{k_j k_{j-1}}. \tag{6}$$

4. Results and discussion

We employed the SERPENT-2 Monte Carlo code to calculate all parameters herein. We used the ENDF/B-VII.0 (Chadwick et al., 2006) cross section library for all calculations in the current work. The statistical error in k_{eff} is ⩽25 pcm. The initial calculation state of a full 3D model of the SD-TMSR is identified by normal operation conditions (see Table 3) and fully withdrawn control rod clusters. The obtained results including excess reactivity, control rod worth, shutdown margin, interference effects (shadowing effects), etc. are discussed below.

4.1. Excess reactivity

The excess reactivity ρ_e is calculated by using Eq. 1 at zero burnup (steady-state calculation), when all control rods are fully withdrawn. The ρ_e for ^{233}U, reactor-grade Pu, and TRU used as initial fissile material are listed in Table 5. For ^{233}U case (Ashraf et al., 2020) the initial excess reactivity is about 1180 ± 28 pcm, however, the maximum observed excess reactivity is 1344 ± 25 pcm during 60 effective full-power years (EFPY) of operation (see Fig. 7 after ≈ 8 EFPY of operation). The TRU composition includes substantial thermal neutron absorbers, therefore, the SD-TMSR becomes subcritical relatively quickly. Previous studies showed that for promising fueling scenarios (e.g., TRU/^{232}Th), large excess reactivity is required for long-term core operation (Ashraf et al.,

Table 5
The excess reactivity at startup for the SD-TMSR core with different initial fissile materials.

Initial fissile materials	^{233}U	reactor-grade Pu	TRU
ρ_e	1180 ± 28 pcm	2330 ± 30 pcm	4800 ± 35 pcm
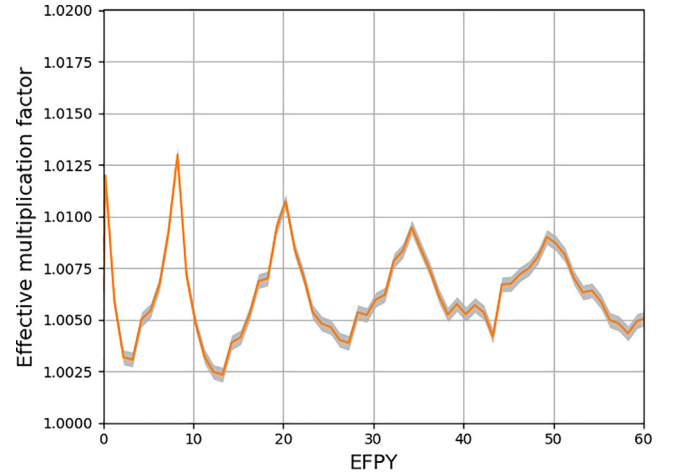
Fig. 7. Uncontrolled effective multiplication factor during 60 EFPY of reactor operation including periodic ^{233}U/^{232}Th insertion (confidence interval $\pm\sigma$ is shaded) (Ashraf et al., 2020).

2020; Betzler et al., 2017; Rykhlevskii et al., 2019). The proposed reactivity control system must compensate such reactivity at startup and during burnup.

4.2. Control rod parameters

The control rod parameters including control rod worth (CRW), interference between CR clusters, and integral and differential control rod worths are described in this work. Table 6 shows calculated CRW and the amplification factor (A_{CRi}) for six different absorbers. The types of interference for all different absorbers are listed in Table 7. Fuel salt composition of LiF–BeF$_2$–ThF$_4$-^{233}UF$_4$ at 70–17.5–12.3–0.2 mol% is used to generate the results listed in Tables 6 and 7. However, Table 8 summarizes the CRW of all CRs, CSD, and SSD for SD-TMSR initially loaded by reactor-grade Pu and TRU.

4.2.1. CRW

Among the absorbers investigated, the total worth of all CRs extends from 10558 ± 30 pcm to 14978 ± 37 pcm (the first row in Table 6). B$_4$C-90 (boron enriched to 90% ^{10}B) has the largest absorption ability, while Gd$_2$O$_3$ has the lowest absorption compared with the other absorbing materials in this study. This result agrees with macroscopic absorption cross section data (Guo et al., 2019). B$_4$C-90 has the highest macroscopic absorption cross section followed by Eu$_2$O$_3$, natural B$_4$C (Nat. B$_4$C), HfB$_2$, HfH$_{1.62}$, and finally Gd$_2$O$_3$. The CR material is being transmuted during operation; the effect of the fuel salt burnup on the CRW is neglected herein and will be investigated in future work.

The worth of the Control Safety Devices (CSD) clusters is 1.56 times greater than the worth of the Shutdown Safety Devices (SSD) system for all absorbing materials. Either CSD or SSD clusters are able to shut down the reactor initially loaded by ^{233}U regardless of the absorbing material type. For reactor-grade Pu (Table 8), also, either CSD or SSD clusters are able to compensate the initial excess

Table 6
The control rod worth for different CR materials (SD-TMSR initially loaded by ^{233}U).

Control Rod group	Nat. B$_4$C		B$_4$C-90		HfB$_2$		HfH$_{1.62}$		Gd$_2$O$_3$		Eu$_2$O$_3$	
	$\Delta\rho_{CRi}$ [pcm]	A_{CRi}	$\Delta\rho_{CRi}$ [pcm]	A_{CRi}	$\Delta\rho_{CRi}$ [pcm]	A_{CRi}	$\Delta\rho_{CRi}$ [pcm]	A_{CRi}	$\Delta\rho_{CRi}$ [pcm]	A_{CRi}	$\Delta\rho_{CRi}$ [pcm]	A_{CRi}
All control rods	13067 ± 35		14978 ± 37		12739 ± 35		11576 ± 31		10558 ± 30		13596 ± 35	
CSD	6990 ± 29	1.22 ± 0.01	7914 ± 28	1.26 ± 0.01	6534 ± 28	1.27 ± 0.01	6490 ± 29	1.16 ± 0.01	5705 ± 25	1.18 ± 0.01	7080 ± 28	1.26 ± 0.01
SSD	4482 ± 31	1.35 ± 0.02	4998 ± 34	1.41 ± 0.02	4400 ± 35	1.41 ± 0.01	4034 ± 29	1.26 ± 0.06	3805 ± 28	1.28 ± 0.01	4676 ± 35	1.39 ± 0.02
CSD inner ring	5011 ± 42	1.61 ± 0.01	5704 ± 47	1.70 ± 0.04	4951 ± 47	1.56 ± 0.02	4804 ± 38	1.53 ± 0.01	4306 ± 38	1.57 ± 0.01	5068 ± 31	1.76 ± 0.01
CSD outer ring	635 ± 31	3.87 ± 0.06	836 ± 35	4.16 ± 0.07	602 ± 27	4.26 ± 0.10	554 ± 30	3.94 ± 0.06	550 ± 29	3.31 ± 0.14	681 ± 28	3.75 ± 0.05
CSD2	660 ± 30	4.10 ± 0.08	692 ± 31	4.44 ± 0.16	694 ± 32	3.61 ± 0.10	610 ± 29	3.33 ± 0.03	553 ± 28	3.68 ± 0.20	685 ± 29	4.26 ± 0.08
CSD9	111 ± 18	7.82 ± 0.10	127 ± 29	7.63 ± 0.01	99 ± 20	10.10 ± 0.05	87 ± 19	6.13 ± 0.10	82 ± 25	9.74 ± 0.20	115 ± 19	10.83 ± 0.10
SSD1	1257 ± 25	1.41 ± 0.01	1290 ± 27	2.09 ± 0.08	1205 ± 30	2.05 ± 0.07	1104 ± 25	1.77 ± 0.01	1071 ± 27	2.02 ± 0.08	1224 ± 31	2.33 ± 0.01
SSD4	183 ± 32	10.18 ± 0.10	179 ± 25	10.68 ± 0.15	191 ± 35	7.78 ± 0.10	298 ± 37	7.51 ± 0.16	188 ± 36	6.96 ± 0.27	185 ± 25	10.43 ± 0.28

reactivity or shut down the reactor initially loaded by reactor-grade Pu regardless of the absorbing material type. However, only SSD clusters made of B$_4$C-90 are able to shut down the SD-TMSR initially loaded by transuranic (TRU) elements (ρ_e is 4800 ± 35 pcm). The reason for this is the much larger absorption cross section of ^{10}B in the relatively soft neutron energy spectrum of the SD-TMSR core started with TRU (Ashraf et al., 2020).

The inner ring of the CSD is located in the central zone of the SD-TMSR core (Fig. 5), in which the volume ratio between molten salt and graphite is relatively small (0.357). Results show that the inner ring of the CSD has a worth almost equal to the worth of all other CRs together (SSD + CSD outer ring) regardless of the absorbing material type (see Table 6). This happens because the absorption cross section decreases with the energy of the incident neutron; for example, boron absorbs neutrons in the thermal spectrum much greater than in the fast spectrum. Additionally, the maximum neutron flux is located in the central zone of the SD-TMSR (see Fig. 9); therefore, the inner ring of the CSD has a worth higher than the worth of the outer ring of the CSD.

In case of malfunction of other CR clusters (e.g., stuck in the upper position), the outer ring of the CSD will be able to compensate the excess reactivity of the core initially loaded by ^{233}U. Meanwhile, it will fail to compensate the excess reactivity of the core initially loaded by reactor-grade Pu and TRU elements. In this unlikely case, the fuel salt temperature will rise, melt a freeze plug, and hot salt will be drained into subcritical drain tanks to safely shut down the reactor.

We separately calculated the worth of CSD2, CSD9, SSD1, and SSD4 clusters (i.e., clusters located in the center and at the boundary between the core zones, see Fig. 5) to investigate the variation of CRW with the position in the inner core. The CRW decreases in the direction of the outer core zone. The outer core zone has smaller moderator-to-fuel ratio (0.86) compared with the central zone (2.80); consequently, the neutron energy spectrum is faster in the peripheral zone than in the center of the core degrading the CR's absorption ability in that region.

4.2.2. Shutdown margin (SDM)

The Shutdown Safety Devices (SSD) clusters are designed mainly for an emergency shutdown, thus it should provide the reactor core with sufficient negative reactivity. The shutdown margin (SDM) is calculated by Eq. 3. Table 9 summarizes the shutdown margins for the SD-TMSR core initially loaded with ^{233}U, reactor-grade Pu, and TRU elements for different absorbing materials. All absorbing materials provide a sufficient positive SDM for the SD-TMSR core that is initially loaded with ^{233}U and reactor-grade Pu. We considered the sufficient positive SDM to be 2β, where β is the total fraction of delayed neutron precursors. Thus, the sufficient positive SDM is ~1300 pcm. The SDMs for the TRU case are negative or slightly positive (in B$_4$C-90 case). Thus, the SSD clusters made of non-B$_4$C-90 materials are ineffectual to shut down the reactor loaded with TRU. Table 10 lists the shutdown margin provided by all SSD clusters when a single SSD cluster with maximum worth (i.e., SSD1) is withdrawn. As shown in Table 10, the control rods still meet the shutdown requirement even in the case of SSD1 cluster failure (withdrawal) for the SD-TMSR core that is initially loaded with ^{233}U and reactor-grade Pu. For the TRU case, in the case of SSD1 cluster failure, substitutional insertion of CSD with SSD clusters will provide a sufficient positive SDM.

4.2.3. Interference between CR systems

The amplification factor (A_{CRi}) results show that the CSD, SSD, CSD inner ring, and SSD1 are slightly amplified due to the anti-shadowing effects. The anti-shadowing is observed when the combined rod worth is greater than the sum of the individual worths.

Table 7
The shadowing effect for different CR materials (SD-TMSR initially loaded by ^{233}U).

Control Rod group	Nat. B$_4$C Interference	B$_4$C-90 Interference	HfB$_2$ Interference	HfH$_{1.62}$ Interference	Gd$_2$O$_3$ Interference	Eu$_2$O$_3$ Interference
CSD	☆	☆	☆	☆	☆	☆
SSD	☆	☆	☆	☆	☆	☆
CSD inner ring	☆	☆	☆	☆	☆	☆
CSD outer ring	☆	☆	☆	☆	☆	☆
CSD2	☆	☆	☆	☆	☆	☆
CSD9	☆☆	☆☆	☆☆	☆☆	☆☆	☆☆
SSD1	☆	☆	☆	☆	☆	☆
SSD4	☆☆	☆☆	☆☆	☆☆	☆☆	☆☆

☆ anti-shadowing effects observed.
☆☆ strong anti-shadowing effects observed.

Table 8
The CRW of all CRs, CSD, and SSD for SD-TMSR initially loaded by reactor-grade Pu and TRU, unit [pcm].

Absorbingmaterials	Startup fissile material					
	Pu			TRU		
	All CRs	CSD	SSD	All CRs	CSD	SSD
Nat. B$_4$C	11353 ± 35	5963 ± 30	3908 ± 31	12173 ± 31	6872 ± 35	4408 ± 30
B$_4$C-90	13264 ± 35	6755 ± 29	4837 ± 35	13915 ± 30	7883 ± 28	5028 ± 35
HfB$_2$	10825 ± 27	5562 ± 30	3741 ± 31	12027 ± 30	6795 ± 31	4477 ± 29
HfH$_{1.62}$	9836 ± 30	4828 ± 32	3545 ± 30	11651 ± 30	6583 ± 31	4158 ± 30
Gd$_2$O$_3$	8608 ± 35	4384 ± 28	3471 ± 31	10356 ± 28	5851 ± 29	3858 ± 31
Eu$_2$O$_3$	11826 ± 31	6019 ± 30	4073 ± 29	12648 ± 30	7146 ± 30	4604 ± 31

As listed in Tables 6 and 7, the strongest anti-shadowing effect occurred in SSD4 and CSD9 clusters that are located at the boundary between the core zones with different moderator-to-fuel ratios. This happened because fewer clusters surround the SSD4 and CSD9 clusters compared with other clusters located in the inner zone of the SD-TMSR (see Fig. 5). Consequently, low interference between these SSD4 and CSD9 clusters and other surrounding clusters is observed. The obtained results show a negligible relationship between the absorbing material type and the interference between the CR clusters (i.e., the A$_{CRi}$).

We calculated the shutdown margin (SDM) and the amplification factor (A$_{CRi}$) for three different configurations of the CRs in the graphite element. The SD-TMSR initially loaded by TRU was selected for this analysis due to the maximum excess reactivity at startup. As shown in Fig. 8, the three rods in the graphite element save the 60-degree symmetry of the component; however,

results show that the SDM in such a case is −1058 pcm and the A$_{CRi}$ is 1.09. In the case of four rods, the 60-degree symmetry of the graphite element is broken; however, the SDM is about 228 pcm, and the A$_{CRi}$ is 0.97. Finally, when six rods are distributed evenly in the graphite element, both symmetry and relatively high SDM are obtained (598 pcm), but the A$_{CRi}$ is about 0.29, which means high interference between rods due to the shadowing effect in this case. Therefore the 3- and 6-CRs configurations are ineffectual due to the negative SDM and the low A$_{CRi}$, respectively. The 4-CRs configuration is adopted in the current study since the SDM is positive, and almost no shadowing effect has been observed.

Insertion of the CR affects the neutron flux distribution, which is the primary reason for the amplification of CRWs indicated in Table 6. Fig. 9 illustrates the radial neutron flux distribution at the mid-core level with different CR positions: (1) all CRs withdrawn, (2) all CRs inserted, (3) all CSD inserted, (4) all SSD inserted.

Table 9
The SDMs for the SD-TMSR core for different absorbing materials.

Absorbing materials	^{233}U	reactor-grade Pu	TRU
Nat. B$_4$C	3302 ± 28 pcm	1743 ± 31 pcm	−392 ± 25 pcm
B$_4$C-90	3818 ± 30 pcm	2507 ± 39 pcm	228 ± 26 pcm
Eu$_2$O$_3$	3496 ± 30 pcm	1645 ± 25 pcm	−196 ± 25 pcm
HfB$_2$	3220 ± 42 pcm	1412 ± 42 pcm	−323 ± 25 pcm
HfH$_{1.62}$	2854 ± 35 pcm	1215 ± 31 pcm	−642 ± 31 pcm
Gd$_2$O$_3$	2625 ± 41 pcm	1141 ± 31 pcm	−942 ± 35 pcm

Table 10
The SDMs for the SD-TMSR core when the SSD1 cluster is fully withdrawn.

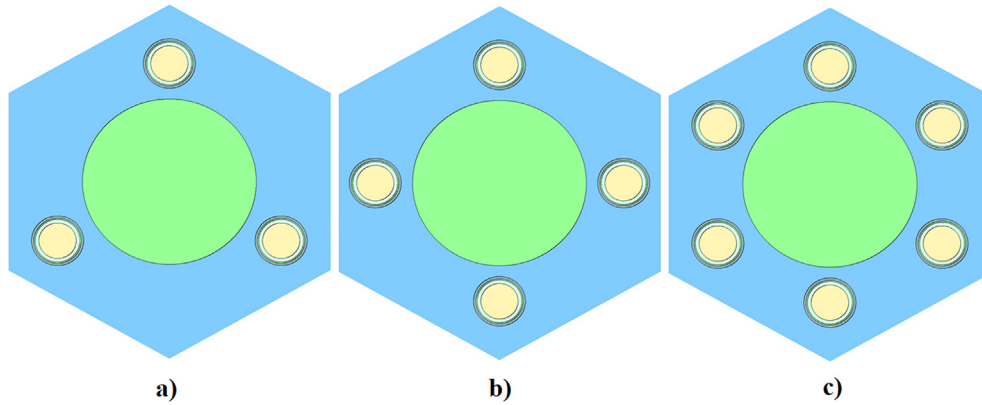| Absorbing materials	^{233}U	reactor-grade Pu	TRU
Nat. B$_4$C	2045 ± 25 pcm	498 ± 27 pcm	−1637 ± 27 pcm
B$_4$C-90	2528 ± 25 pcm	1257 ± 25 pcm	−1082 ± 26 pcm
Eu$_2$O$_3$	2272 ± 30 pcm	524 ± 27 pcm	−1450 ± 25 pcm
HfB$_2$	2015 ± 35 pcm	257 ± 37 pcm	−1698 ± 35 pcm
HfH$_{1.62}$	1750 ± 25 pcm	170 ± 27 pcm	−1787 ± 31 pcm
Gd$_2$O$_3$	1554 ± 35 pcm	120 ± 25 pcm	−2166 ± 35 pcm

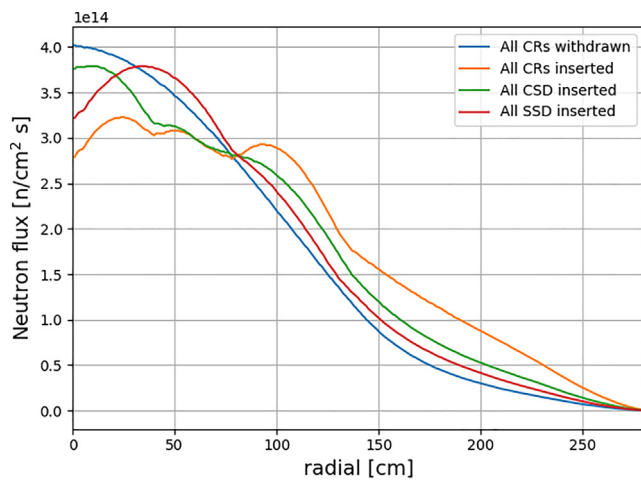**Fig. 8.** *XY section of graphite element with a) 3-CRs b) 4-CRs c) 6-CRs configurations.*

Fig. 9. Radial neutron flux distribution at the mid-core for different CR positions (CRs made of B$_4$C-90).

Fig. 10. Integral CRW of all CRs, CSD, and SSD clusters (CRs made of B$_4$C-90).

We chose the B$_4$C-90 as the absorbing material because of its high absorption ability. As shown in Fig. 9, the insertion of CRs deforms the radial flux shape close to CRs. This shifts the neutron flux from the core center towards the periphery. The maximum neutron flux shift occurs when all CRs are inserted into the core (Girardin et al., 2007).

4.2.4. Integral and differential CRW

The integral CRWs are calculated for three different systems: all CRs, CSD, and SSD systems. We calculated the differential CRWs for the CSD system only because special adjusting rods (i.e., CSD) were assumed to adjust the reactivity. The CRs are inserted gradually into the core from the top to the bottom. Eqs. 5 and 6 are used to calculate the integral and differential CRW, respectively. Fig. 10 illustrates the integral CRW for CRs made of B$_4$C-90. The maximum integral worth of all CRs, CSD, and SSD clusters are about 14978 *pcm*, 7914 pcm, and 4998 pcm, respectively. The integral worth of SSD clusters made of B$_4$C-90 is sufficient to shut down the reactor from any state.

The differential CRWs are demonstrated in Fig. 11. Theoretically, at the top of the core, the CR insertion has little effect since this region has low thermal neutron flux. Thus the differential CRW has the lowest values in this region. The effect of CR insertion increases gradually near the center of the core. At the center of the core (region with maximum thermal neutron flux), the differential CRW is the largest and changes slowly with rod insertion. From the
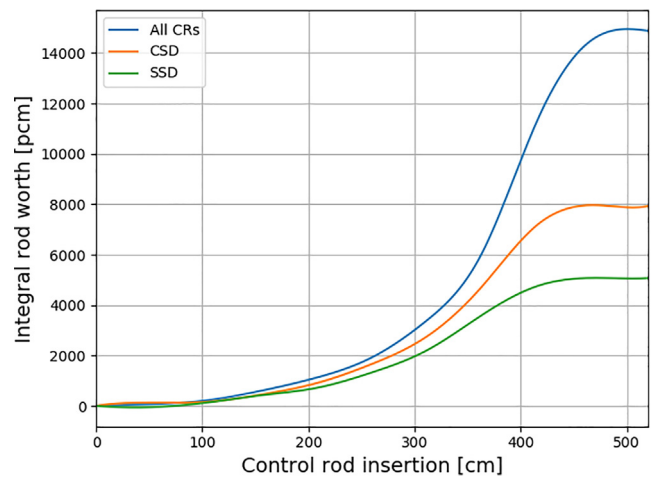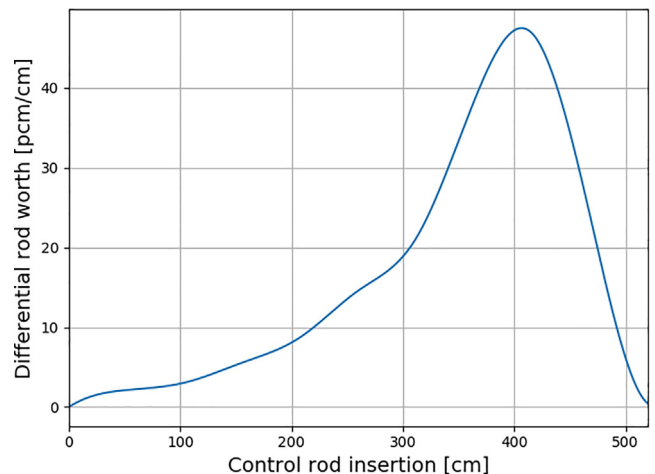

Fig. 11. Differential CRW of CSD clusters (CRs made of B$_4$C-90).

center of the core to the bottom, the differential CRW values decrease (region with low thermal neutron flux). Fig. 11 shows that the maximum differential CRW is shifted toward the bottom of the core and the curve is not exactly symmetrical. This is due to the asymmetrical distribution of the fuel and graphite in simulation (Xuemei and Guimin, 2013; Son et al., 2016).
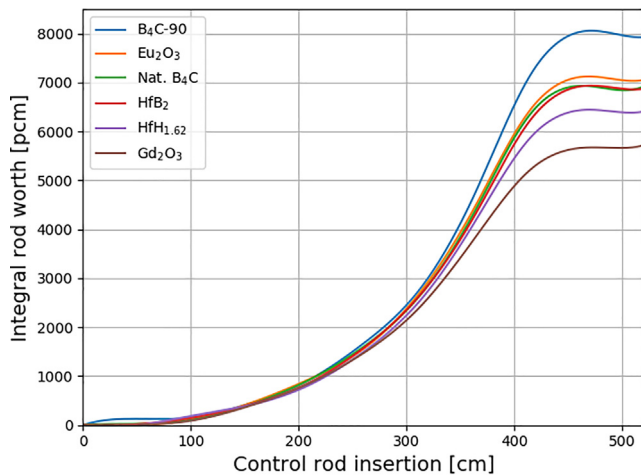
Fig. 12. Integral CRW of CSD clusters for various absorbing materials.

Fig. 12 shows the integral CRW for only Control Safety Devices (CSD) clusters with six different absorbing materials. The results show that all absorbing materials have almost the same integral rod worth in the upper half of the core (< 250 cm from the upper boundary of the core). Further insertion of the CRs demonstrates that the strongest absorber, B_4C-90 outperforms other materials. Notably, all results are based on steady-state calculations.

5. Conclusion

In the current work, we proposed a first-ever reactivity control system design based on control rods in addition to the online feed system reactivity control in the Single-fluid Double-zone Thorium-based Molten Salt Reactor (SD-TMSR). The design has been evaluated at the startup for a full 3D model of the SD-TMSR using the SERPENT-2 Monte-Carlo code. We considered three startup fuel salt compositions: (1) ^{232}Th as fertile and ^{233}U as fissile material; (2) ^{232}Th and Pu, extracted from LWR SNF; (3) ^{232}Th and TRU, extracted from LWR SNF.

The excess reactivity ρ_e is calculated at zero burnup when all CRs are fully withdrawn. The ρ_e for ^{233}U, reactor-grade Pu, and TRU are 1180 ± 28 pcm, 2330 ± 30 pcm, and 4800 ± 35 pcm, respectively.

Six different absorbing materials are considered in this work: natural B_4C, B_4C-90 (boron is enriched to 90% ^{10}B), HfB_2, $HfH_{1.62}$, Eu_2O_3, and Gd_2O_3. Enriched B_4C-90 has the largest absorption ability, while Gd_2O_3 has the lowest absorption compared with the other absorbing materials in this study. Both Control Safety Devices (CSD) and Shutdown Safety Devices (SSD) clusters are separately able to shut down the reactor initially loaded with ^{233}U and reactor-grade Pu regardless of the absorbing material type. However, only SSD clusters made of B_4C-90 are able to shut down the SD-TMSR initially loaded with TRU from LWR. The reason for this is the much larger absorption cross section of ^{10}B in the relatively soft neutron energy spectrum of the SD-TMSR core started with TRU.

In case of malfunction of the other CR clusters (e.g., stuck in the upper position), the outer ring of the CSD failed to counteract the excess reactivity of the core initially loaded with reactor-grade Pu and TRU elements. Therefore, the fuel salt temperature will rise, melt a freeze plug, and hot salt will be drained into subcritical drain tanks to safely shut down the reactor. However, the worth of the outer ring of the CSD is sufficient to compensate the excess reactivity for the core refueled by ^{233}U.

All absorbing materials provide an adequate shutdown margin for the SD-TMSR core that initially loaded with ^{233}U and reactor-

grade Pu. However, the shutdown margins for TRU case are negative or slightly positive (in B_4C-90 case). For the TRU case, in the case of SSD1 cluster failure, substitutional insertion of CSD with SSD clusters will provide a sufficient positive SDM.

The amplification factor (A_{CRi}) results show that the CSD, SSD, CSD inner ring, and SSD1 are slightly amplified due to the anti-shadowing effects. The strongest anti-shadowing effect has observed in SSD4 and CSD9 clusters that are located at the boundary between the core zones with different moderator-to-fuel ratios. This happened because fewer clusters surround the SSD4 and CSD9 clusters compared with other clusters located in the inner zone of the SD-TMSR.

The insertion of CRs deforms the radial flux shape close to CRs. This shifts the neutron flux from the core center towards the periphery.

The integral CR worths are calculated for three different systems: all CRs, CSD, and SSD systems, however, the differential CR worths are calculated for only CSD clusters. The results show that all absorbing materials have almost the same integral rod worth in the upper half of the core. Further insertion of the CRs shows the unique absorption characteristics of each material.

Finally, the proposed design of CRs successfully control the excess reactivity and enhance the safety aspects of the SD-TMSR.

6. Future work

The authors intend to evaluate the effect of the fuel salt depletion on the CRW. The depleted fuel composition will be obtained using a SERPENT-2 online reprocessing subroutine and batch-wise tool SaltProc (Rykhlevskii et al., 2018). The xenon poison effect will be studied in our upcoming article when calculating the worth of the control rods during fuel depletion. Additionally, the authors intend to investigate kinetic parameters' (effective delayed neutron fraction β_{eff} and effective delayed neutron precursor decay constant λ_{eff}) evolution during the SD-TMSR operation. These parameters are crucial for accident transient analysis, which will be performed using Moltres (Lindsay et al., 2018), a multi-physics application for liquid-fueled MSR simulation which takes into account the neutron precursors drift.

References

DOE, US, 2002. A technology roadmap for Generation IV nuclear energy systems, pp. 48–52..

Betzler, B.R., Rykhlevskii, A., Worrall, A., Huff, K., 2019. Impacts of Fast-Spectrum Molten Salt Reactor Characteristics on Fuel Cycle Performance, Tech. rep., Oak Ridge National Lab. (ORNL), Oak Ridge, TN (United States)..

Ashraf, O., Rykhlevskii, A., Tikhomirov, G., Huff, K.D., 2020. Whole core analysis of the single-fluid double-zone thorium molten salt reactor (sd-tmsr). Ann. Nucl. Energy 137,. https://doi.org/10.1016/j.anucene.2019.107115. URL: http://www.sciencedirect.com/science/article/pii/S0306454919306255 107115.

Nuttin, A., Heuer, D., Billebaud, A., Brissot, R., Le Brun, C., Liatard, E., Loiseaux, J.-M., Mathieu, L., Meplan, O., Merle-Lucotte, E., et al., 2005. Potential of thorium molten salt reactorsdetailed calculations and concept evolution with a view to large scale energy production. Progr. Nucl. Energy 46 (1), 77–99.

Elsheikh, B.M., 2013. Safety assessment of molten salt reactors in comparison with light water reactors. J. Radiat. Res. Appl. Sci. 6 (2), 63–70.

Robertson, R.C., 1971. Conceptual Design Study of a Single-Fluid Molten-Salt Breeder Reactor., Tech. Rep. ORNL–4541, comp. Oak Ridge National Laboratory, Tenn. (Jan. URL: http://www.osti.gov/scitech/biblio/4030941.

Ashraf, O., Rykhlevskii, A., Tikhomirov, G., Huff, K.D., 2020. Strategies for thorium fuel cycle transition in the sd-tmsr. Ann. Nucl. Energy 148 (107656). https://doi.org/10.1016/j.anucene.2020.107656.

Betzler, B.R., Robertson, S., Davidson, E.E., Powers, J.J., Worrall, A., 2017. Assessment of the neutronic and fuel cycle performance of the transatomic power molten salt reactor design, ORNL/TM-2017/475, Oak Ridge National Laboratory..

Rykhlevskii, A., Betzler, B.R., Worrall, A., Huff, K.D., 2019. Fuel Cycle Performance of Fast Spectrum Molten Salt Reactor Designs. In: Proceedings of Mathematics and Computation 2019. American Nuclear Society, Portland, OR.

Rykhlevskii, A., Bae, J.W., Huff, K.D., 2019. Modeling and simulation of online reprocessing in the thorium-fueled molten salt breeder reactor. Ann. Nucl. Energy 128, 366–379. https://doi.org/10.1016/j.anucene.2019.01.030.

Betzler, B.R., Powers, J.J., Worrall, A., 2016. Modeling and simulation of the start-up of a thorium-based molten salt reactor, in: Proc. Int. Conf. PHYSOR..

Ashraf, O., Smirnov, A.D., Tikhomirov, G.V., 2019. J. Phys: Conf. Ser. 1189,. https://doi.org/10.1088/1742-6596/1189/1/012007 012007.

Ashraf, O., Tikhomirov, G.V., 2020. J. Phys: Conf. Ser. 1439,. https://doi.org/10.1088/1742-6596/1439/1/012005 012005.

Čerba, Š., Vrban, B., Lüley, J., Nečas, V., Haščík, J., 2017. Optimization of the heterogeneous gfr 2400 control rod design. Prog. Nucl. Energy 97, 170–181.

Atkinson, S., Litskevich, D., Merk, B., 2019. Small modular high temperature reactor optimisation part 2: Reactivity control for prismatic core high temperature small modular reactor, including fixed burnable poisons, spectrum hardening and control rods. Prog. Nucl. Energy 111, 233–242.

N.R. Commission, et al., 1987. Standard review plan for the review of safety analysis reports for nuclear power plants: Lwr edition, Tech. rep., Nuclear Regulatory Commission..

Guo, H., Buiron, L., Kooyman, T., Sciora, P., 2019. Optimized control rod designs for Generation IV fast reactors using alternative absorbers and moderators. Ann. Nucl. Energy 132, 713–722.

Li, G.C., Cong, P., Yu, C.G., Zou, Y., Sun, J.Y., Chen, J.G., Xu, H.J., 2018. Optimization of Th-U fuel breeding based on a single-fluid double-zone thorium molten salt reactor. Prog. Nucl. Energy 108, 144–151. https://doi.org/10.1016/j.pnucene.2018.04.017. URL: http://www.sciencedirect.com/science/article/pii/S0149197018300970.

Zou, C., Cai, C., Yu, C., Wu, J., Chen, J., 2018. Transition to thorium fuel cycle for tmsr. Nucl. Eng. Des. 330, 420–428.

Zhang, A., Zou, C., Wu, J., Xia, S., Yu, C., Chen, J., 2020. Radiotoxicity of minor actinides in thermal, epithermal and fast tmsrs with very high burnup. Ann. Nucl. Energy 137, 107162.

Briesmeister, J.F., et al., 2000. Mcnptm-a general monte carlo n-particle transport code, Version 4C, LA-13709-M, Los Alamos National Laboratory 2..

Mathieu, L., Heuer, D., Brissot, R., Garzenne, C., Le Brun, C., Lecarpentier, D., Liatard, E., Loiseaux, J.-M., Meplan, O., Merle-Lucotte, E., et al., 2006. The thorium molten salt reactor: moving on from the msbr. Prog. Nucl. Energy 48 (7), 664–679.

Xuemei, Z., Guimin, L., 2013. Study of control rod worth in the tmsr 24 (1). 10601–010601.

Petrie, L.M., Landers, N.F., 1984. Keno va: an improved monte carlo criticality program with supergrouping, Tech. rep..

Leppänen, J., Pusa, M., Viitanen, T., Valtavirta, V., Kaltiaisenaho, T., 2013. The serpent monte carlo code: status, development and applications in 2013. In: SNA+ MC 2013-Joint International Conference on Supercomputing in Nuclear Applications+ Monte Carlo. EDP Sciences, p. 06021.

Jiang, M., Xu, H., Dai, Z., 2012. Advanced fission energy program-tmsr nuclear energy system. Bull. Chin. Acad. Sci 27 (3), 366–374.

Li, X., Cai, X., Jiang, D., Ma, Y., Huang, J., Zou, C., Yu, C., Han, J., Chen, J., 2015. Analysis of thorium and uranium based nuclear fuel options in fluoride salt-cooled high-temperature reactor. Prog. Nucl. Energy 78, 285–290.

Marka, J.C., 1993. Explosive properties of reactor-grade plutonium. Sci. Global Secur. 4 (1), 111–128.

de Saint Jean, C., Delpech, M., Tommasi, J., Youinou, G., Bourdot, P., 2000. Scénarios cne: réacteurs classiques, caractérisation à l'équilibre, rapport CEA DER/SPRC/LEDC/99-448..

Ashraf, O., Tikhomirov, G., 2020. Thermal-and fast-spectrum molten salt reactors for minor actinides transmutation. Ann. Nucl. Energy 148, 107751.

Séran, J.-L., Flem, M.L., 2017. 8 – irradiation-resistant austenitic steels as core materials for Generation IV nuclear reactors. In: Yvon, P. (Ed.), Structural Materials for Generation IV Nuclear Reactors. Woodhead Publishing, pp. 285–328. https://doi.org/10.1016/B978-0-08-100906-2.00008-2.

Chadwick, M., 2006. Endf/b-vii0: next generation evaluated nuclear data library for nuclear science and technology. Nucl. Data Sheets 107 (12), 2931–3060. https://doi.org/10.1016/j.nds.2006.11.001. URL: http://www.sciencedirect.com/science/article/pii/S0090375206000871.

Oka, Y., 2014. Nuclear reactor design. Springer Japan.

Girardin, G., Rimpault, G., Coddington, P., Chawla, R., 2007. Control rod shadowing and antishadowing effects in a large gas-cooled fast reactor. In: Proceedings of ICAPP, vol. 7, pp. 13–18..

Son, N.A., Hoa, N.D., Nguyen, T.T., Tuan, T.Q., Raul, O.C., 2016. Control rod calibration and worth calculation for optimized power reactor 1000 (opr-1000) using core simulator opr1000. World J. Nucl. Sci. Technol. 7 (1), 15–23.

Rykhlevskii, A., Bae, J.W., Huff, K., 2018. arfc/saltproc: Code for online reprocessing simulation of molten salt reactor with external depletion solver SERPENT, Zenododoi:10.5281/zenodo.1196455.https://zenodo.org/record/1196455#.WqrE_BPwaA0..

Lindsay, A., Ridley, G., Rykhlevskii, A., Huff, K., 2018. Introduction to Moltres: an application for simulation of Molten Salt Reactors. Ann. Nucl. Energy 114, 530–540. https://doi.org/10.1016/j.anucene.2017.12.025.